LCLS-II Technical Note

LCLS-II TN Photon Collimators – Fault Signal Generation and Detection

LCLS-II TN-17-07

3/6/17

Yiping Feng

1 Introduction

Certain error conditions (system faults) may arise in the accelerator causing the Free-electron laser (FEL) beam to stray from its nominal path of propagation and impinge on surfaces of beamline components that are not designed to handle either the peak FEL fluence or the average FEL power. If not properly mitigated, these fault conditions, even if existing momentarily, could cause permanent damages to those components. As such, a large number of collimators will be strategically placed along the beamline to corral the FEL beam and to prevent it from hitting any unintended components. For the LCLS-II high repetition rate beams, a new collimator design different from that implemented for the LCLS 120 Hz machine is required, and is shown schematically in Figure 1,. The complete physics requirements and the functional requirements specification can be found in LCLSII-3.5-PR-0051-R1 and LCLSII-3.5-FR-0543-R2, respectively.

Each collimator is designed to have a fault detection mechanism connected to the Machine Protection System (MPS) and/or Beam Containment System (BCS), from which further corrective actions can be issued and taken. Since the MPS response time from a positive fault detection to the moment that the beam is turned off or steered back to its nominal trajectory is finite and is designed to be ≤ 100 μs, each collimator could be temporarily irradiated by the full FEL beam for up to the MPS response time and must remain undamaged. The collimators are *not* required to handle the full FEL beam indefinitely as in the case of the photon stoppers. The collimator fault detection mechanism, depicted in

Figure 2, is implemented by detecting X-ray scatterings from the FEL beam striking the collimator surface. It has the additional beam position monitoring (BPM) capability by using multiple and spatially separated diodes. Furthermore, based on readings from two or more collimator/BPM's located sufficiently apart, the pointing of the FEL beam could be evaluated.

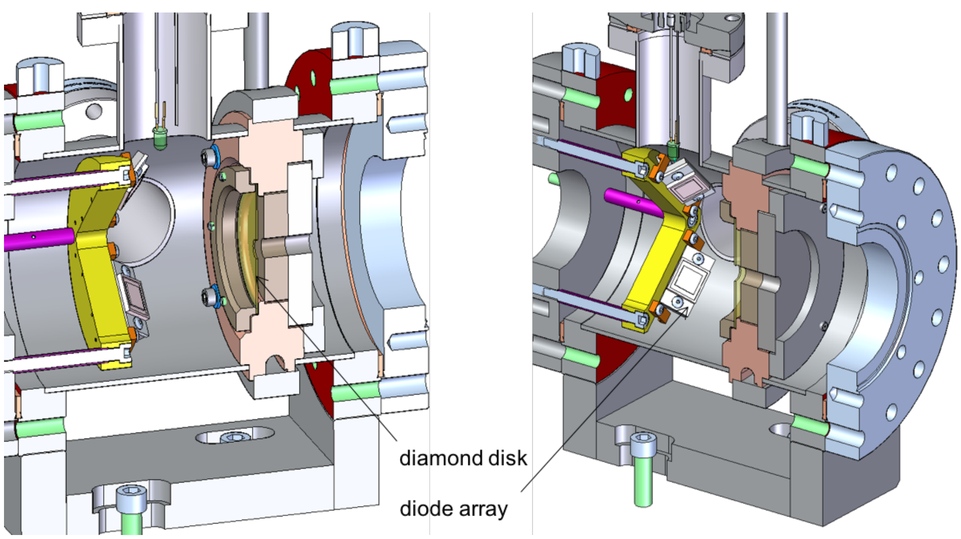

Figure 1. Schematics of the collimator's fault detection/BPM conceptual design. The graphite-coated diamond disk provides the damage protection for downstream beamline components. In the event of a miss-steered beam the back scattered X-ray will be detected by a 4-diode array (only

two are shown) positioned upstream of the diamond disk, generating a fault signal. The 4 diodes are divided into two independent groups for redundancy.

1.1. Mode of Operation

In the event of a miss-steered FEL beam, the X-ray pulses would strike at near normal incidence* onto the graphite-coated diamond surface as depicted in

Figure 2, and the FEL beam is either partially clipped or fully absorbed. A certain percentage of the X-rays would be back scattered (both the coherent Thomson and incoherent Compton scattering processes will be present) and detected by a 4-diode detector array positioned at a distance *z* mm upstream of the diamond disk. The 4 diodes mounted off beam axis by distance *R* mm (designated as top and bottom, and left and right) and are pitched at 45° from the horizontal with no roll or jaw rotations (< 0.5°) as shown Figure 2. The diodes are square in shape and have 10x10 mm^2 in active surface area. The 4 separate outputs from the diodes will be used to ***a***) generate the signal for the fault condition, ***b***) to provide the relative beam position in relation to the collimator assembly, and ***c***) as an option to assess the approximate pointing error of the beam when used in conjunction with readings from two or more collimator/BPM devices.

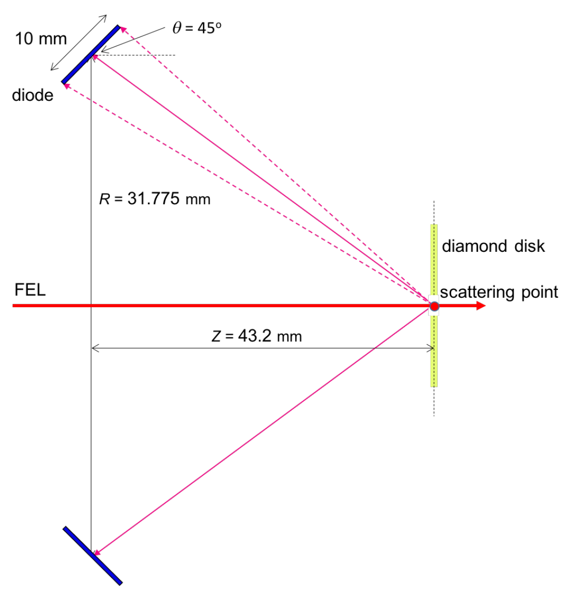

Figure 2. Dimensions of the diodes and the diamond disk for the fault signal calculation. The back scattered X-rays from the surface in the event of a miss-steer are detected by a 4-diode array. The raw signals from the 4 quadrature diodes are separately amplified and converted into intensity readings I_1 through I_4.

1.1.1. Measurement of the Fault Signals

The most important measurement of the fault detection assembly (diodes and associated electronics) is to generate two independent fault signals for redundancy:

$$I_{fault-1} = I_1 + I_2$$

* The FEL beam is extremely collimated even in the lower energy range of the soft X-rays, any deviation from the normal trajectory is only a fraction of a mrad.

$$I_{fault-2} = I_3 + I_4$$

…… Eqn. (1)

where I_1 and I_2 are the signals from the top-left and bottom-left diodes of the array as depicted in

Figure 2, and I_3 and I_4 are the signals from the top-right and bottom-right diodes. The fault signals will be sent to two separate comparators for deciding the onset of a faulty condition, and will also be converted to digital signals for calculating the position of the miss-steered beam relative to the collimator assembly described in Section 1.1.2.

1.1.2. Measurement of the Relative Beam Transverse Positions

As an additional capability, the digital signals from the 4 diodes will be used to estimate roughly beam positions:

$$X = C_X \frac{(I_1 + I_2) - (I_3 + I_4)}{I_{total}}$$

$$Y = C_Y \frac{(I_1 + I_3) - (I_2 + I_4)}{I_{total}}$$

…… Eqn. (2)

where X and Y are the horizontal and vertical positions of the FEL beam in the plane normal to the beam propagation, and $I_{\text{total}} = \Sigma I_i$ is the total intensity of all 4 diodes. Due to the linear polarization of the FEL beam, the scattered X-ray intensity profile exhibits anisotropy in the azimuthal angle (see discussion in the Appendix), resulting dissimilar proportional constants for C_X and C_Y, but must be calibrated. *In-situ* calibration of C_X and C_Y represents practical challenges due to the pulse-by-pulse jitters in intensity, position, and beam pointing of the FEL beam.

1.1.3. Angular Measurement

Based on reading from two or more collimators/BPM's, the pointing of the FEL beam can be estimated using:

$$\alpha \cong tan\alpha = \frac{X_1 - X_2}{\Delta z}$$

$$\beta \cong tan\beta = \frac{Y_1 - Y_2}{\Delta z}$$

…… Eqn. (3)

where α and β are the take-off angles of the FEL beam from the nominal trajectory, respectively, X_j and Y_j are horizontal and vertical positions of the j-th monitor for j = 1, and 2, and Δz the distance between collimator 1 and 2.

2. Fault Signal Generation and Detection

2.1. Scattering Calculations

2.1.1. Scattering Materials

The working materials of the collimators that provide the protection for the downstream beamline components are graphite and diamond. The diamond disk is the main material capable of sustaining a high power FEL beam such as generated by the LCLS-II, but is coated with a thin (~ 2 μm) graphite layer to mitigate the potential single-shot damage of the diamond in the energy range of at and above the carbon *K*-edge of 284.2 eV, where the X-ray absorption cross-section is much higher and the process of graphitization could commence if diamond is heated instantaneously above its graphitization temperature of ~ 1400 K, corresponding to an atomic dose of ~ 0.213 eV/atom. Especially for collimator units closer to the FEL source point, this graphitization threshold can be easily surpassed based on the latest Start-to-End FEL performance simulations (c.f., refer to most updated LCLS-II FEL performance documents). Outside this graphitization range and at higher photon energies, the attenuation by the graphite layer is relatively small, the diamond will "see" the FEL beam. As such, either graphite or a graphite/diamond combination will generate scattering signals should the FEL beam strike the collimator surface.

2.1.2. Dose Calculations

2.1.2.1. Peak Atomic Dose

The peak dose ε, defined as the maximum amount of energy absorbed per atom irradiated by a Gaussian beam of waist size ω_0, is given by

$$\varepsilon_{max} = \max\left(\lim_{\Delta V\to 0}\int \frac{\Delta E}{\Delta N}dt\right) = \left.\frac{h\upsilon I_0 \Delta T e^{-\frac{2r^2}{\omega_0^2}} e^{-\frac{z}{L_{pe}}}}{L_{pe}\left(\frac{\pi\omega_0^2}{2}\right)n}\right|_{z=0,r=0} = \frac{h\upsilon I_0\Delta T}{L_{pe}\left(\frac{\pi\omega_0^2}{2}\right)n}$$

…… Eqn. (4)

where ΔE is the energy absorbed per unit time in volume $\Delta V = 2\pi r\Delta r\Delta z$, having $\Delta N = n\Delta V$ atoms, n being the atomic number density (atoms/unit volume), $I_0\Delta T$ is the total number of photons integrated over the duration of the pulse ΔT, L_{pe} is the (photoelectric) attenuation length at photon energy $h\nu$, h being the Planck constant. Other beam loss mechanisms with the exception of the photoelectric effect are neglected.

The peak dose calculated in Eqn. (4) depends on the size of the beam, thus will vary from collimator to collimator with the most upstream collimator receiving the maximum peak dose in the entire transport, unless the FEL beam is focused to a smaller size, such as after focusing devices. The dose can be expressed in terms of the atomic cross-section and peak fluence by the following relation

$$\varepsilon_{max} = = \frac{h\upsilon I_0\Delta T}{L_{pe}\left(\frac{\pi\omega_0^2}{2}\right)n} = \frac{E_{pulse}}{\left(\frac{\pi\omega_0^2}{2}\right)}\sigma_{pe} = F_{max}\sigma_{pe}$$

…… Eqn. (5)

where F_{max} is the maximum fluence, and σ_{pe} is the atomic cross-section for the photoelectric effect to be calculated in Section 2.1.4.

2.1.2.2. Graphitization/Melting Threshold

The graphitization threshold can be calculated using a thermodynamic model whereby the absorbed energy contained in the fast photoelectrons would eventually be thermalized with the lattice and converted to energies in the translational, vibrational, and rotational degrees of freedom. The time scale of the thermalization is roughly given by that of the electron-phonon interactions, and is much faster than the thermal diffusion time. As such the absorbed energy remains localized, causing the temperature at the interaction point to rise by an amount equal to the specific heat integrated over the same temperature span.

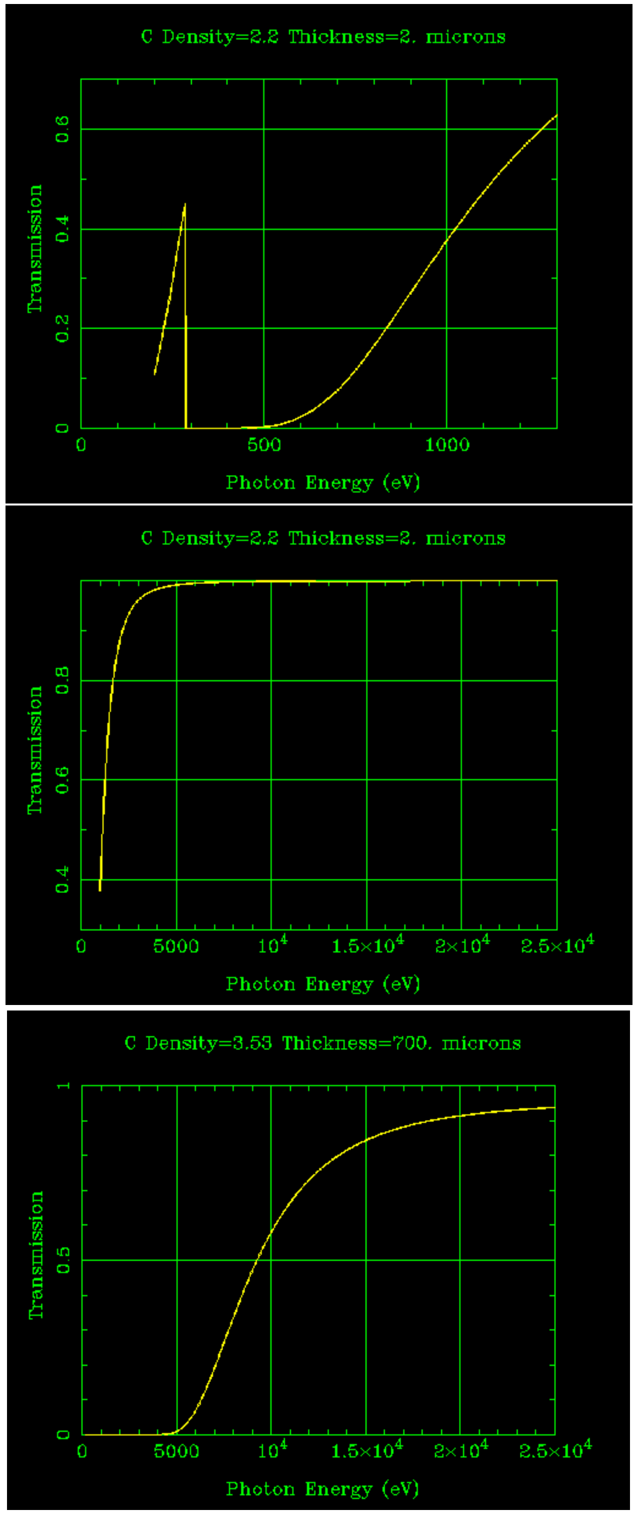

Figure 3. The percentage of X-rays beam transmitting through the graphite layer and reaching the diamond for the soft X-ray (top) and hard X-ray (middle) cases. The carbon *K*-edge is evidenced by the

peak near 284.4 eV. The percentage of X-rays transmitting through the graphite layer and the diamond for the hard X-ray (bottom) case. As such, for energies < 5 keV, the FEL beam will be completely (> 99%) attenuated if intercepted by the collimator.

2.1.3. Transmission through Graphite Layer and Diamond Disk

The percentage of the X-ray beam transmitting through the graphite layer depends on the photon energy, assuming near normal incidence, is shown in Figure 3 for the soft X-ray collimators (top) and hard X-ray collimators (middle). The transmission is independent of the size of the FEL beam. The near zero transmission is evidenced by the carbon *K*-edge at 284.4 eV and approximately 200 eV beyond.

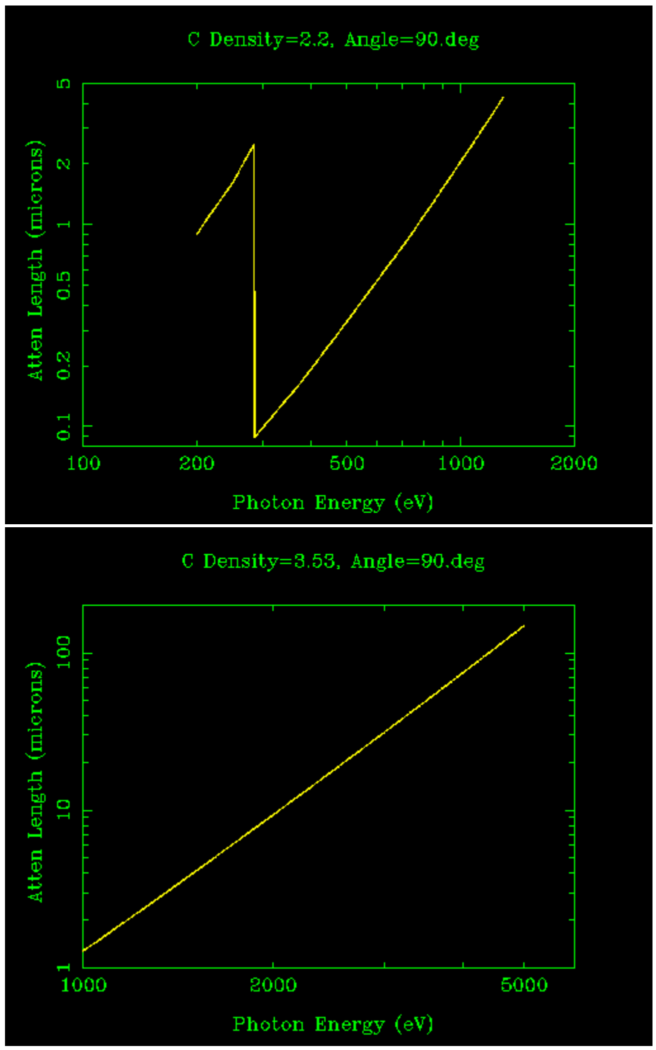

Figure 4. The attenuation length of graphite (top, density 2.2 g/cc) and diamond (bottom density 3.53 g/cc) used to estimate the total effective thickness of material involved in the scattering processes. At the carbon *K*-edge near 284.4 eV, only ~ 88 nm worth of carbon atoms is doing the scattering, as opposed to ~ 239 μm (equivalent to ~149 μm of diamond) at 5 keV, a drastic difference of more than 2700 times that makes the design more challenging.

For the hard X-ray FEL, the remaining intensity reaching the diamond disk and then transmitting through is shown in the bottom panel of Figure 3. For energies < 5 keV, > 99% of the FEL beam is attenuated if intercepted by the collimator, and the amount of carbon atoms in the graphite layer and/or the diamond disk involved in the scattering, however, is limited only to those within one attenuation length, not the entire sample thickness. For energies > 5 keV, if the absorption length exceeds the diamond thickness, then SiC disk behind the diamond must also be taken into account. This additional consideration is not covered here, but a rough estimate is provided.

2.1.4. X-ray Scatterings

2.1.4.1. Scattering Processes

The total scattered X-rays into the diode array include contributions from three principal scattering processes: Compton (incoherent and inelastic) scattering, Rayleigh (coherent and elastic) scattering, and X-ray fluorescence (incoherent). The dominant fluorescence signal comes from the radiative process filling the core holes created by the photoelectric effect. For light elements such as carbon (graphite and diamond), the florescence yield is rather low. The detector will also receive electronic signals from photoelectrons as well as electrons escaping the bulk material via secondary processes such as the Auger process. Other effects such as pair-production or nuclear excitations are small in the energy range considered and are thus ignored. Not considered are other re-excitation and re-emission processes, or non-linear processes which may or may not be important in the present application.

1.1.1.1. Scattering Geometry

The diodes are in the back scattering geometry as shown in Figure 1. This is based on the consideration that avoiding non-diffusive effects such as diffractions or other coherent scatterings from a fully transverse coherent FEL beam favors the choice of putting the X-ray detectors in the back scattering geometry, resulting in a larger scattering vector that would minimize the coherent scattering contributions. The angular distribution of the incoherent scattering, on the other hand, is much more homogeneous, thus helping minimize potential spurious scattering events into the detectors that might cause false trips.

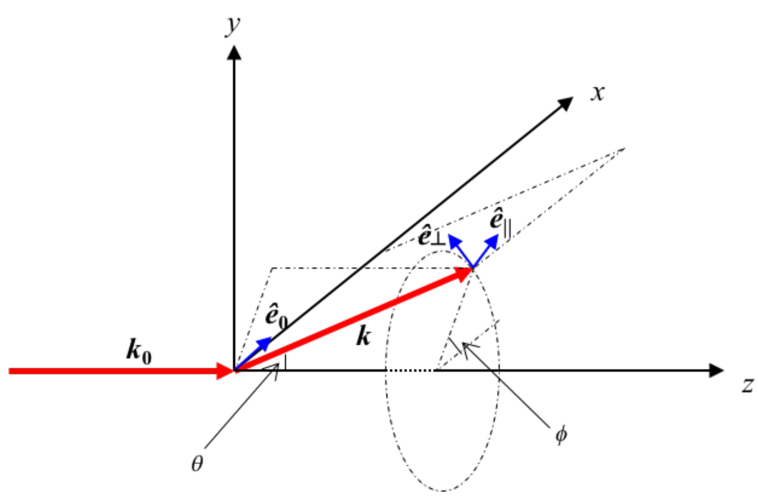

Figure 5. Scattering Geometry where the incident X-ray polarization $\hat{\boldsymbol{e}}_0$ is in the horizontal direction (only for the soft X-ray branch, but the physical picture remains the same for the hard X-ray branch with a vertical polarization). The scattering angle θ is between the incident wavevector $\boldsymbol{k}_0$ and the scattered wavevector $\boldsymbol{k}$. The azimuth angle ϕ is between the ($\hat{\boldsymbol{e}}_0$, $\boldsymbol{k}_0$) plane and the ($\boldsymbol{k}$, $\boldsymbol{k}_0$)

plane. The elastically scattered radiation is polarized in the ($\hat{\boldsymbol{e}}_0$, $\boldsymbol{k}_0$) plane and perpendicular to the scattered wavevector $\boldsymbol{k}$, and is indicated by the vector $\hat{\boldsymbol{e}}_{||}$, whereas the inelastically scattered is unpolarized and has components in $\hat{\boldsymbol{e}}_{||}$ and $\hat{\boldsymbol{e}}_{\perp}$, which is normal to the ($\hat{\boldsymbol{e}}_0$, $\boldsymbol{k}_0$) plane.

1.1.1.2. Scattering Cross-Sections

The atomic scattering cross-section for carbon has been calculated for Rayleigh scattering, Compton scattering, X-ray fluorescence, and the primary photoelectrons from the photoelectric effect. The incident X-rays are assumed to propagate in the direction of the z-axis, and polarized in the direction of the x-axis as shown in Figure 5. The results of a complete calculation are provided in the appendix for reference. Below we summarize the main findings for all scattering and electronic processes:

i. The angular distribution of the integrated cross-section over the azimuth angle ϕ and a finite polar angular range of $\Delta\theta$ (= π/180) for Rayleigh scattering, Compton scattering, and the sum are shown in Figure 6 as a function of the scattering angle θ. In the angular range between θ = 138º to 149º where the diodes are located, the coherent Rayleigh process complete dominates at low energies of 1 keV, whereas at high energies approaching 24.8 keV, it is quite negligible compared to the incoherent Compton process. At 8.3 keV, the two processes contribute approximately equally. The percentage of the Rayleigh contribution to total scattering varies from ~ 100% at low energies to a few % at higher energies. The combined back scatterings have a broad local maximum in the vicinity of θ = 135º. To have positional sensitivity, the detector elements were set at angles where there are large angular variations.

ii. The angular distributions of the differential cross-section of Rayleigh and Compton scatterings as a function of the scattering angle θ are shown in Figure 7 (top) and (bottom) panels, respectively at a photon energy of 1 keV. Both the Rayleigh and the Compton processes show polarization effects in the azimuth angle characteristic of a linearly polarized incident FEL beam. At θ = 90º, the scattered intensity displays dipolar behavior with zero intensity nodes at ϕ = 0º and 180º.

iii. The angular distributions of the differential cross-section of Rayleigh and Compton scatterings as a function of the scattering angle ϕ are shown in Figure 8 (top) and (bottom) panels, respectively at a photon energy of 1 keV. Both the Rayleigh and the Compton processes show polarization effects in the azimuth angle characteristic of a linearly polarized incident FEL beam.

iv. The angular distribution of the K-fluorescence from a collection of large number of atoms is uniform in 4π solid angles, although the emission process (a delayed and spontaneous emission of an excited atom) from a given atom is dipolar in nature given by its instantaneous dipole moment at the exact moment of emission (delayed with respect to the scattering processes).

v. The angular distribution of the primary electrons is highly anisotropic, characteristic of a dipolar transition, arising from the $\boldsymbol{p}\bullet\boldsymbol{A}$ term in the interaction Hamiltonian. Most electrons are distributed along the polarization of the incident X-rays, i.e. θ = 90º and ϕ = 0º. The primary electrons are prompt, so no averaging over large number of atomic orientation is warranted.

vi. The angular distribution of the Auger-electrons from a collection of large number of atoms is uniform in 4π solid angles is assumed to be uniform in 4π, although the decay process (a delayed process with respect to the scattering processes) from a given atom should be anisotropic; the overall distribution should be obtained by averaging over many atoms of having random orientations for the outgoing electrons.

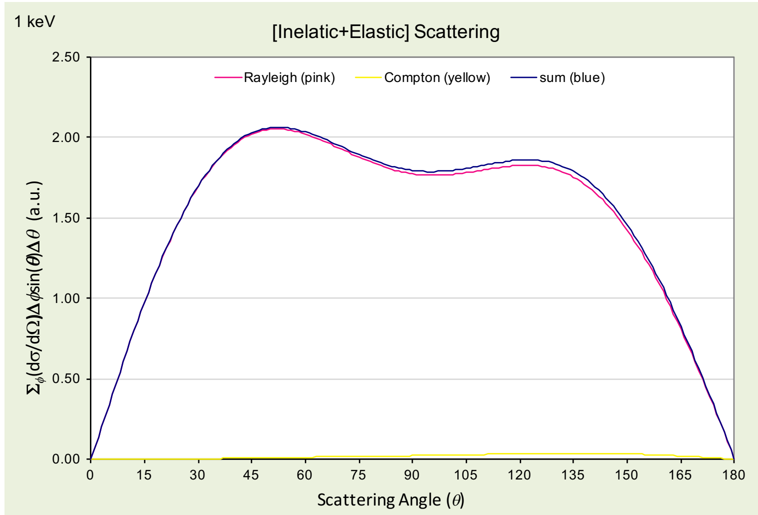

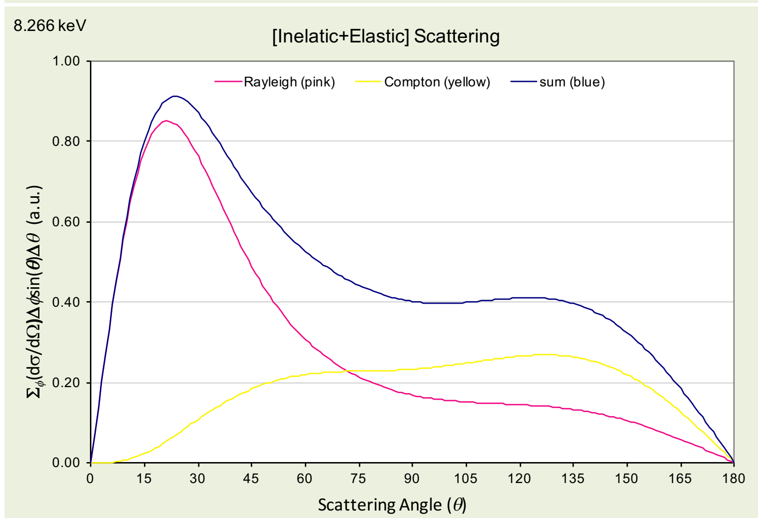

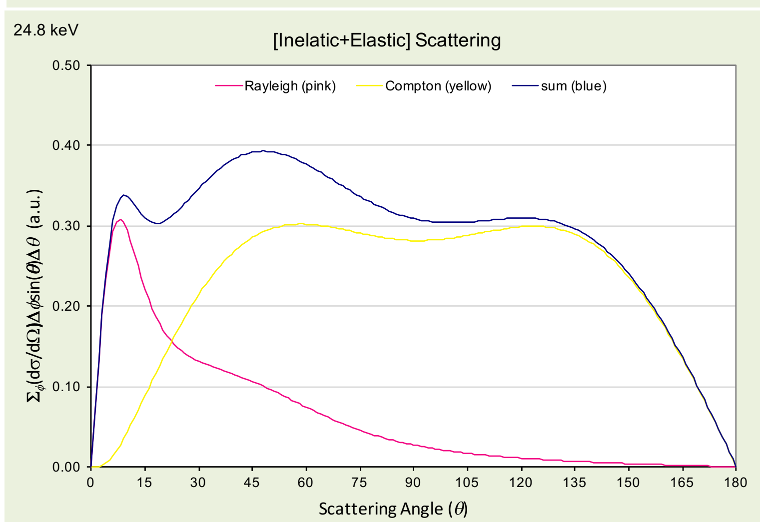

Figure 6. Angular distribution as a function of the scattering angle θ of the combined (Rayleigh & Compton) scattering cross-section (blue), the inelastic Compton (yellow) and the elastic Rayleigh (pink) scattering contributions at 1 keV (top), 8.3 keV (middle), and 24.8 keV (bottom) for carbon.

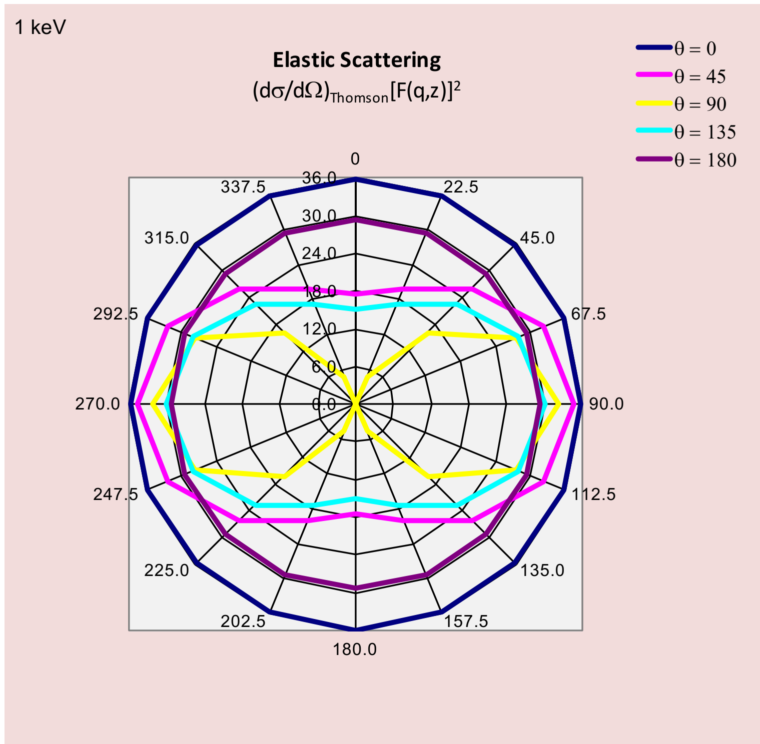

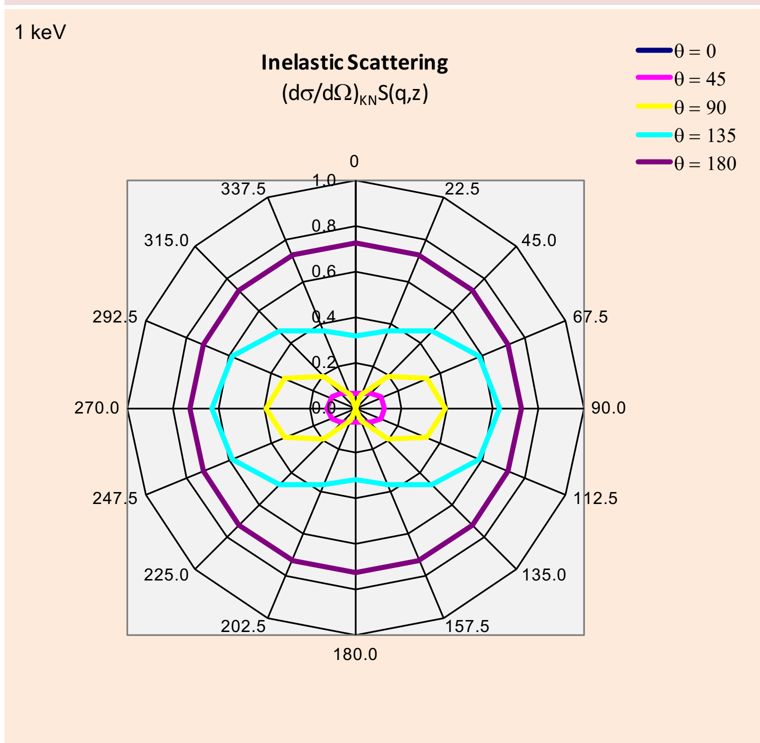

Figure 7. Angular distribution in azimuth angle ϕ of the differential cross-section of the total Rayleigh (top) and Compton scattering (bottom) at a fixed scattering angle θ for Carbon at a photon energy of 1 keV. The ϕ dependence exhibits two-fold and inversion symmetries.

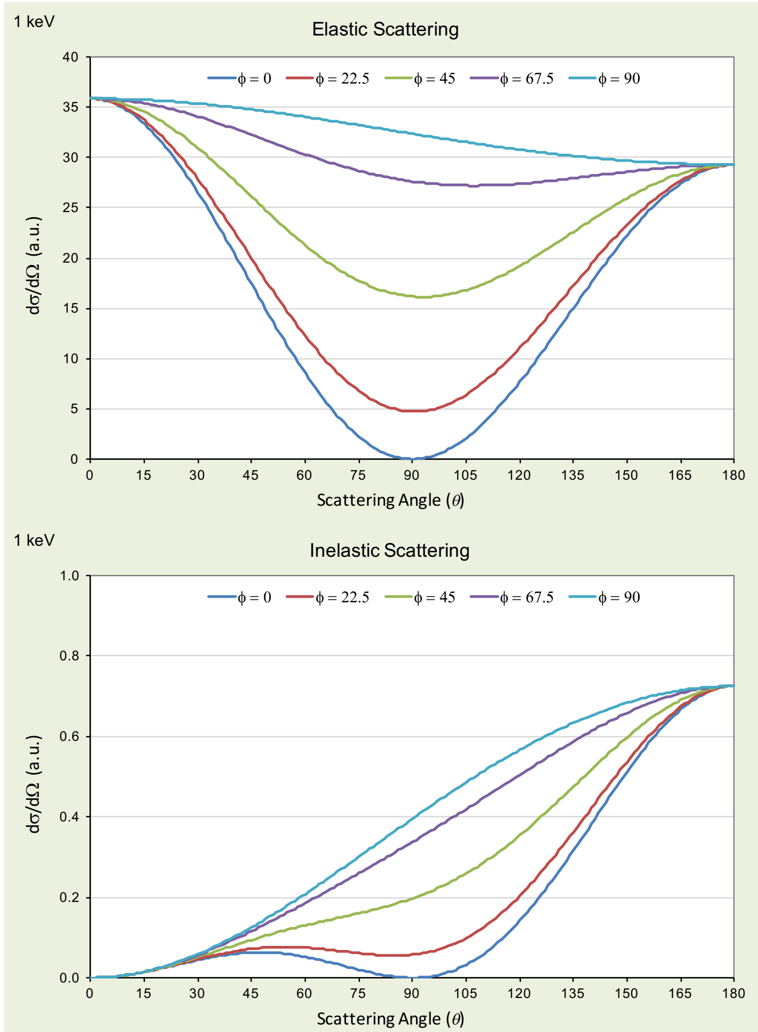

Figure 8. Angular distribution in scattering angle θ of the differential cross-section of the total Rayleigh (top) and Compton scattering (bottom) at a fixed azimuth angle ϕ for Carbon at a photon energy of 1 keV. The scattered intensity has zero intensity at $\theta = 90^{\circ}$ for $\phi = 0^{\circ}$ or 180° (not shown).

1.1.1.3. Back Scattering Intensity

The total intensity from both Rayleigh and Compton scattering (photons/pulse) scattered onto the detector elements, ignoring multiple scattering, is given by

$$I_{total} = \int_{0}^{L} I_{inc}^{0} e^{-\frac{z}{L_0}} \int_{\theta_1}^{\theta_2} \int_{\phi(\theta)_1}^{\phi(\theta)_2} \left(\frac{d\sigma}{d\Omega}\right)(\theta,\phi)\, d\phi \sin\theta\, d\theta \rho dz$$

$$= I_{inc}^{0}\rho\left[1 - e^{-\frac{L}{L_0}}\right] L_0 \int_{\theta_1}^{\theta_2} \int_{\phi(\theta)_1}^{\phi(\theta)_2} \left(\frac{d\sigma}{d\Omega}\right)(\theta,\phi)\, d\phi \sin\theta\, d\theta$$

$$= I_{inc}^{0}\rho \int_{\theta_1}^{\theta_2} \int_{\phi(\theta)_1}^{\phi(\theta)_2} \left(\frac{d\sigma}{d\Omega}\right)(\theta,\phi)\, d\phi \sin\theta\, d\theta \times \begin{cases} L, if\ L \ll L_0 \\ L_0, if\ L \gg L_0 \end{cases}$$

…… Eqn. (6)

where ρ and L are the density (gm/cm^3) and effective carbon thickness of the graphite/diamond combination layer (cm), L_0 the attenuation length (cm) of at a given energy of the graphite, I_{inc}^0 the incident FEL intensity (photons/pulse), and finally ($d\sigma/d\Omega$) the total scattering cross-section in units of cm^2/gm. In the thin layer limit, the scattered intensity scales linearly with the effective thickness L, but in the thick layer limit, the intensity is proportional to the attenuation length L_0 because the scattering gets weaker while the beam is being attenuated. The integrations in ϕ and θ are in principle trivial to carry out regardless of the shape of the diodes, but approximations can be made due to the limited angular range that the angle dependent cross-section ($d\sigma/d\Omega$) can be taken outside of the integral.

$$I_{total} = I_{inc}^{0}\rho \int_{\theta_1}^{\theta_2} \int_{\phi(\theta)_1}^{\phi(\theta)_2} \left(\frac{d\sigma}{d\Omega}\right)(\theta,\phi)\, d\phi \sin\theta\, d\theta \times \begin{cases} L, if\ L \ll L_0 \\ L_0, if\ L \gg L_0 \end{cases}$$

$$\approx I_{inc}^{0}\rho \left(\frac{d\sigma}{d\Omega}\right)(\theta_0,\phi_0)\Delta\Omega \times \begin{cases} L, if\ L \ll L_0 \\ L_0, if\ L \gg L_0 \end{cases}$$

…… Eqn. (7)

where $\Delta\Omega = A/R^2$ is the approximate solid angle subtended by the diode (θ_0, ϕ_0), referenced to the center of the graphite/diamond disk, with A and R being the surface area of the diode and the distance from the disk to the diode, respectively.

The total cross-section including both Compton and Thomson processes have been calculated and shown in the top panel of Figure 9, integrated over the 4π solid angle in the units of cm^2/g, and the bottom panel of that approximated over the solid angle subtended by one diode of 10x10 mm^2 at roughly 53.6 mm from the center of the diamond disk and in the direction of $\theta = 144°$ and $\phi = 45°$. The number of X-ray photons scattered into one diode is then given by:

$$I_{scattered} = I_{inc}^{0}\sigma_{\Delta\Omega} \begin{cases} \rho L, if\ L \ll L_0 \\ \rho L_0, if\ L \gg L_0 \end{cases}$$

…… Eqn. (8)

where I^0_{inc} is the photons/pulse, and ρ in g/cm^3 is the density, and L and L_0 is the thickness and attenuation length in cm, respectively. L_0 is given in Figure 4 for graphite and diamond. For example, at the carbon K-edge, L_0 = 88 nm, and for graphite ρ = 2.2 g/cm^3 and assuming I^0_{inc} = 1x10^{13}/pulse, we have $I_{\text{scattered}}$ = 1.31x10^6/pulse. This is the worst case scenario when the absorption length is the shortest. At any other energies, the signal will be much higher.

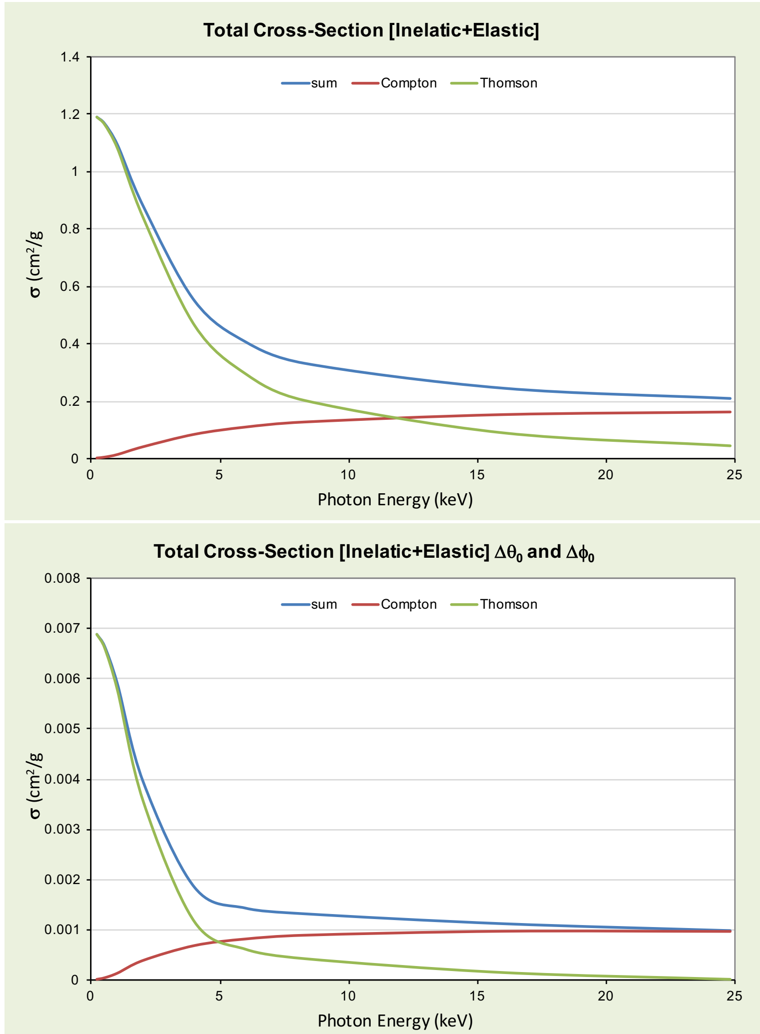

Figure 9. (top) Total scattering cross-section including both the Compton and Thomson processes integrated over the 4π solid angle in the units of cm^2/g. (bottom) Total scattering cross-section including both the Compton and Thomson processes approximated over the solid angle subtended by one diode of 10x10 mm^2 at roughly 53.6 mm from the center of the diamond disk and in the direction of $\theta = 144°$ and $\phi = 45°$.

1.1.2. *K*-Fluorescence

1.1.2.1. *K*-fluorescence Cross-section

One of the radiative decay processes following the creation of *K*-shell holes by the incident X-rays is the *K*-shell fluorescence. The fluorescence yield ω_K for *K*-shell electrons can be represented by an empirical equation (M. O. Krause, "Atomic Radiative and Radiationless Yields for K and L Shells," J. Phys. Chem. Ref. Data 8, 307 (1979)) dependent on the atomic number Z (in atomic forms):

$$\ln\left(\frac{1}{\omega_K} - 1\right) = -3.94\ln(Z) + 13.5$$

$$\omega_K = 1.4\times10^{-3}, \qquad Z = 6$$

…… Eqn. (9)

Assuming the K-shell holes are generated by the one-photon photoelectric effect, the total K-fluorescence cross-section in 4π sterradian is given by:

$$\sigma_K = \Sigma_{pe-K}\omega_K$$

…… Eqn. (10)

where Σ_{pe-K} is the total cross-section for the photoelectric effect for generating K-shell hole to be described in Section 1.1.3.1 integrated over 4π.

The angular distribution of the K-fluorescence is assumed to be uniform in 4π solid angles although the emission process (spontaneous emission of an excited atom) from a given atom is dipolar in nature given by its instantaneous dipole moment at the exact moment of emission (delayed with respect to the scattering processes); the overall distribution should be obtained by averaging over many atoms of random dipole orientations.

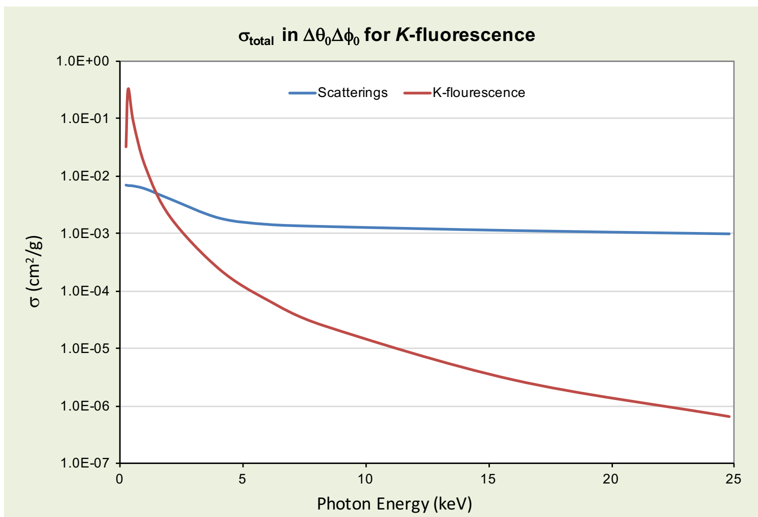

Figure 10. The cross-section of the K-fluorescence (red) integrated over the solid angle subtended by one diode of 10x10 mm^2 at roughly 53.6 mm from the center of the diamond disk and in the direction of $\theta = 144°$ and $\phi = 45°$. The peak corresponds to the carbon K-edge at 284.4 eV. The cross-section for the scattering processes (blue) was included for comparison.

1.1.2.2. *K*-fluorescence Intensity

The total K- fluorescence intensity collected by the multi-element detector is given by

$$I_{total} = I_{inc}^0\rho\int_{\theta_1}^{\theta_2}\int_{\phi(\theta)_1}^{\phi(\theta)_2}\frac{\sigma_K}{4\pi}d\phi\sin\theta\, d\theta\times\begin{cases}L, if\ L \ll L_0\\ L_0, if\ L \gg L_0\end{cases}$$

$$\approx I_{inc}^0\rho\left(\frac{\Sigma_{pe-K}\omega_K}{4\pi}\right)\Delta\Omega\times\begin{cases}L, if\ L \ll L_0\\ L_0, if\ L \gg L_0\end{cases}$$

…… Eqn. (11)

where the same approximation in integration as in Eqn. (7) has been made. The quantity in the parentheses has no angular dependence, indicating the uniformity of K-fluorescence from an ensemble of atoms.

1.1.3. Photoelectron

The total photoelectric cross-section includes contributions from all atomic shells including the *K*-shell and the *L*-shell, with the *K*-shell contribution being the dominant process provided the X-ray energy is high enough, if however, for the soft X-rays in the low energy range, the contributions from other shells should also be taken into account. The primary product of the photoelectric effect is the primary photoelectrons ejected from the atoms whose kinetic energy is simply given by the Einstein relation. These primary electrons are highly energetic and could be scattered again before escaping the bulk material. The decay channels following the photoelectric excitation, i.e. creation of inner shell holes, are secondary processes including radiative *K*-fluorescence described in 1.1.2 and non-radiative Auger processes.

1.1.3.1. Primary Photoelectrons

The differential cross-section for the *K*-shell photoelectrons can be estimated, when the incident X-ray energy is far from an absorption edge, and is highly anisotropic as given by

$$\frac{d\sigma_{pe-K}}{d\Omega} = r_e^2 Z^5 \alpha^4 2^{\frac{5}{2}} \left(\frac{m_e c^2}{h\nu}\right)^{\frac{7}{2}} \sin^2\theta \cos^2\phi$$

…… Eqn. (12)

where $r_e = e^2/m_e c^2 = 2.818\times10^{-13}$ cm, $m_e c^2 = 0.511$ MeV is the electron rest mass, $h\nu$ is the photon energy, and $\alpha = 2\pi e^2/hc = 1/137.035$ is the fine structure constant, the angles θ and ϕ are defined in Figure 5. The total cross-section integrated over the θ and ϕ angles gives a factor of $4\pi/3$. The angular distribution is purely dipolar, arising from the $\boldsymbol{p}\cdot\boldsymbol{A}$ term in the interaction Hamiltonian. The primary photoelectrons are distributed along the polarization of the incident X-rays, i.e. $\theta = 90^\circ$ and $\phi = 0^\circ$.

Assuming no re-scattering of the primary photoelectrons, the total number of primary photoelectrons collected by the diode is given by:

$$I_{total} = I_{inc}^0 \rho \int_{\theta_1}^{\theta_2} \int_{\phi(\theta)_1}^{\phi(\theta)_2} \frac{\sigma_K}{4\pi} d\phi \sin\theta\, d\theta \times \begin{cases} L, if\ L \ll L_0 \\ L_0, if\ L \gg L_0 \end{cases}$$
$$\approx I_{inc}^0 \rho r_e^2 Z^5 \alpha^4 2^{5/2} \left(\frac{m_e c^2}{h\nu}\right)^{7/2} \sin^2\theta_0 \cos^2\phi_0\, \Delta\Omega \times \begin{cases} L, if\ L \ll L_0 \\ L_0, if\ L \gg L_0 \end{cases}$$

…… Eqn. (13)

where the same approximation in integration as in Eqn. (7) has been made, and θ_0 and ϕ_0 are angles of the center of the diode referenced to the center of the graphite/diamond disk, respectively. Since the primary photoelectrons almost always go through re-scattering, Eqn. (13) gives the maximum number of primary electrons that could be seen by the diode.

1.1.3.2. Auger Electrons

The non-radiative decay processes following the creation of *K*-shell holes by the incident X-rays is the Auger process whereby the *K*-shell hole is filled by an outer shell electron and at the same time ejecting another different outer shell electron into the continuum. The Auger yield ω_A is related to the fluorescence yield:

$$\omega_A = 1 - \omega_K$$

…… Eqn. (14)

The total cross-section for the Auger process is then given by:

$$\sigma_A = \Sigma_{pe-K}\omega_A = \sigma_{pe-K}(1-\omega_K) =$$

…… Eqn. (15)

where $\Sigma_{pe\text{-}K}$ is the total cross-section for the photoelectric effect for generating K-shell holes in Eqn. (12) in Section 1.1.3.1 integrated over 4π.

The angular distribution of the Auger electrons is assumed to be uniform in 4π, although the decay process from a given atom should be anisotropic; the overall distribution should be obtained by averaging over many atoms of having random orientations for the outgoing electrons.

Assuming no re-scattering of the Auger electrons, the total number of Auger electrons collected by the multi-element detector is given by:

$$I_{total} = I_{inc}^0\rho \int_{\theta_1}^{\theta_2}\int_{\phi(\theta)_1}^{\phi(\theta)_2} \frac{\sigma_K}{4\pi} d\phi \sin\theta\, d\theta \times \begin{cases} L, if\ L \ll L_0 \\ L_0, if\ L \gg L_0 \end{cases}$$
$$\approx I_{inc}^0\rho\left(\frac{\Sigma_{pe-K}(1-\omega_K)}{4\pi}\right)\Delta\Omega \times \begin{cases} L, if\ L \ll L_0 \\ L_0, if\ L \gg L_0 \end{cases}$$

…… Eqn. (16)

where the integrations over the θ and ϕ angles have been carried out. The quantity in the parentheses has no angular dependence, indicating the uniformity of Auger electrons from an ensemble of atoms. Since the Auger photoelectrons may go through re-scattering, Eqn. (16) gives the maximum number of Auger electrons that could be seen by the diode.

1.2. Detection System

1.2.1. Timing Characteristics of Scattered X-rays

The scattered X-rays will be prompt with respect to the incident FEL beam for both the elastic and inelastic processes. As such, the interaction of the scattered X-rays with any detection element will be time-limited to the pulse width, i.e., < 200 fs. This short interaction time eliminates the possibility of photon counting, thus leaving charge collection as the only viable solution for measuring the intensity of the scattered X-rays.

1.2.2. Charge Collection using Photoelectric Effect

1.2.2.1. Silicon Diode Array

The scattered X-ray intensity can be converted to electric charge signal by virtue of the photoelectric effect, and in the case of a Si diode, the X-rays fall directly onto the Si surface, and are internally converted to electron-hole pairs upon absorption, which then generate a charge pulse under a DC electric bias.

1.2.2.2. Quantum Efficiency

To achieve high conversion rate (Quantum Efficiency) at typical X-ray energies, the thickness of the diode is such that almost all of X-rays are absorbed for conversion, and in the case of Si, it should be a multiple of the attenuation length. In Figure 11, the attenuation length as a function of LCLS-II SXR X-ray energy is shown amounting 69 nm at 200 eV and 6.39 µm at 1.3 keV, and HXR energies 2.68 µm at 1 keV and 1.99 mm at 25 keV, covering 7 orders of magnitude.

For the SXR energies from 200 eV to 1.3 keV, the thickness of the Si layer in the diode could be 10 µm, whilst for HXR energies from 1 to 25 keV, it must be at least hundreds of µm thick. For example, at 25 keV a 400 µm thick Si would still yield 20% efficiency and should be sufficient for our purpose. High *Z* materials (such as GaAs) may be used in place of Si for photoelectric conversion if efficiency becomes an issue. There is also an added benefit that the carrier mobility tends to be a bit higher for GaAs than for Si, although speed is not really a concern here due to the minimum delay time between pulses for LCLS-II high repetition rate FEL is still quite long at 1 µs. For now, we only consider Si based diodes with effective thickness of a one or few hundreds of µm to cover both the SXR and HXR applications.

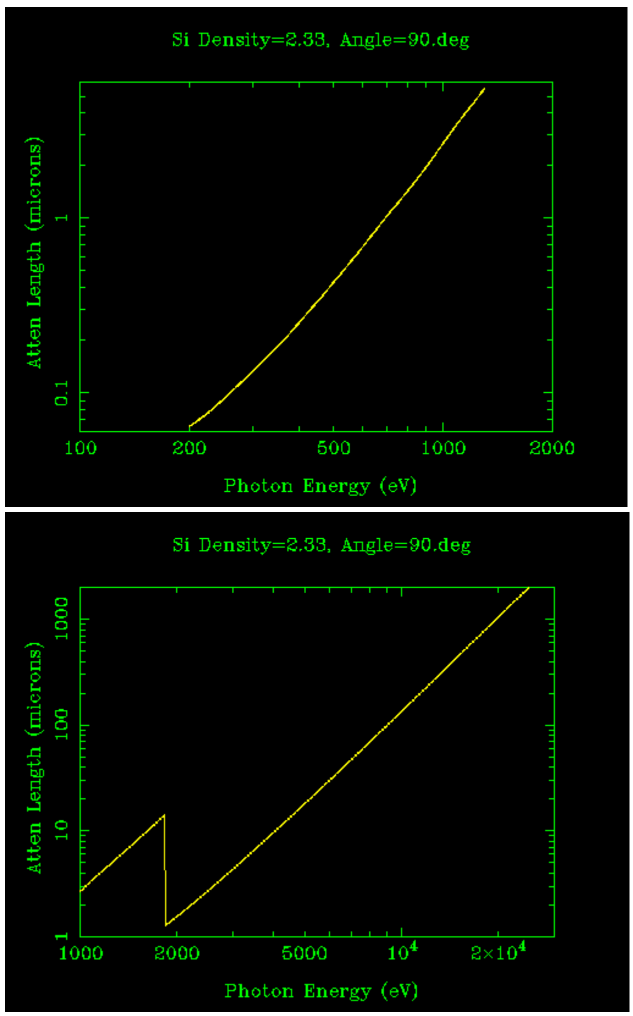

Figure 11. The attenuation length of Si as a function of the LCLS-II SXR X-ray energies (top) and HXR energies (bottom), amounting to 69 nm at 200 eV, 2.68 mm at 1 keV and 1.99 mm at 25 keV and covering a very large dynamic range of 2.8×10^7.

1.2.2.3. Aluminum Coating on Diode

We will put a 50 nm Aluminum coating on the Si diode to make it optically blind to mitigate the concern that bending radiations from the electron dump will send down the beam pipe a lot of optical light so the diodes will always be receiving signals regardless whether or not it is a fault condition. The transmission of the LCLS-II SXR X-rays is shown in Figure 12, which is about 42% at worst at 200 eV.

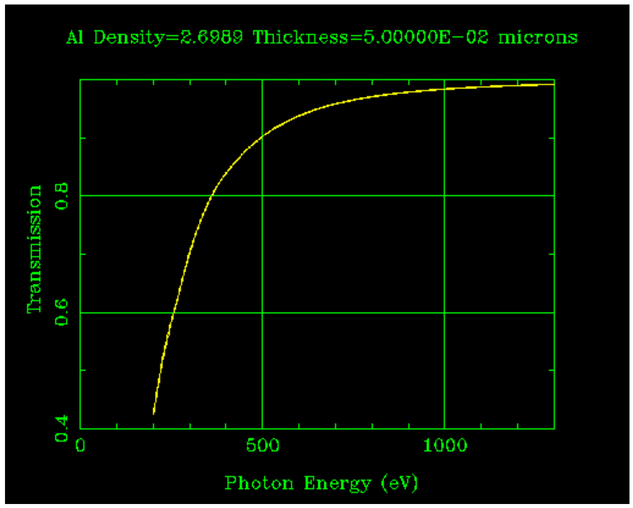

Figure 12. The transmission through a 50 nm layer of aluminum coating on the diode in the LCLS-II SXR X-ray energy range. Above 500 eV, the transmission is above 90% so could be neglected. It does reduce the signal level for energies below 500 eV by a factor of two at worst.

The amount of charge that will be generated in one of the quadrant diodes is plotted in Figure 13, normalized to 1 mJ of FEL intensity and taken into account both the scattering processes in Eqn. (8) and the *K*-fluorescence in Eqn. (13).

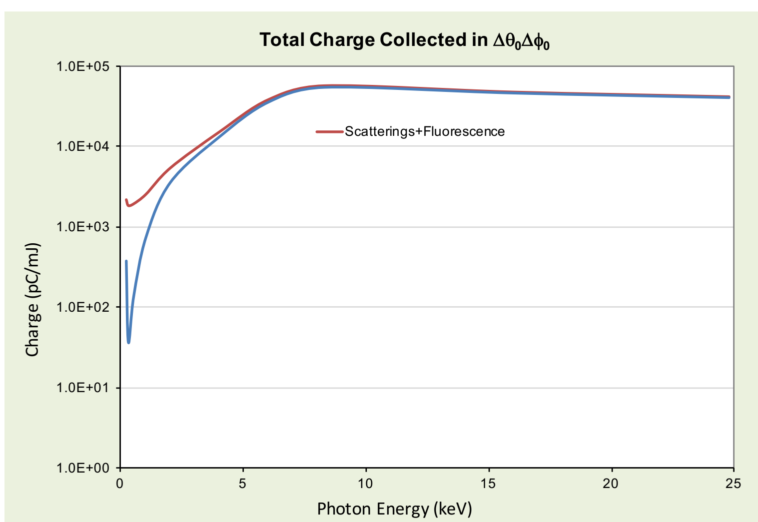

Figure 13. Total charge (red) generated in a diode in units of pC, normalized to 1 mJ of FEL power and taken into account both scatterings processes and *K*-fluorescence. The scattering only signal (blue) is shown for comparison. The *K*-fluorescence makes the response much flatter.

The contributions from primary and Auger electrons are not included, because the direction of the primary electrons will be pointing along the surface of the diamond disk, whilst the Auger electrons will not reach the diodes unless a bias is applied to extract them.

1.2.2.4. Charge Sensitive Amplifier

The number of electron-hole pairs generated by the X-rays is proportional to the energy and for each 62 Å (200 eV) photon and a Si detector, there will be approximately 55 *e-h* pairs (3.62 eV per *e-h* pair) depending on the exact temperature of the sensor. The charge generated at 200 eV is given by:

$$Q_{total} = 55eI_{total} = 8.8\times10^{-6} I_{total}\ (pC)$$

…… Eqn. (17)

where I_{total} is the number of photons falling onto the diode, and Q_{total} is in the units of pC. For the number of photons corresponding to a 5% accuracy from Poisson statistics, say 400, the total charge is about 3.5×10^{-3} pC. For a collection capacitor of 10 pF, this will generate a voltage signal of only 0.35 mV, even without any amplification, this is comparable to noise limit of modern electronics. One concern is the capacitance of the large detection area of the Si diode. For the dimensions specified in the Figure 2, the total capacitance is about 33 pF per diode, larger than the capacitance needed to collect the charge. The amount of charge generated in each diode is quite high and of order nC for 1 mJ of FEL power, so probably too much signal already if the full beam strike the graphite/diamond. So the fault condition will arise even a small part of the beam is hitting the graphite/diamond disk, say, 1%. If using a 1 nF collection capacitor, the total voltage in the diode after the amplifier is plotted in Figure 14, normalized to 1 mJ of FEL power. The voltage will saturate the shaping amplifier, so beam will be tripped much sooner when only small part of the FEL scrapes the graphite/diamond disk. Or a larger capacitor could be used.

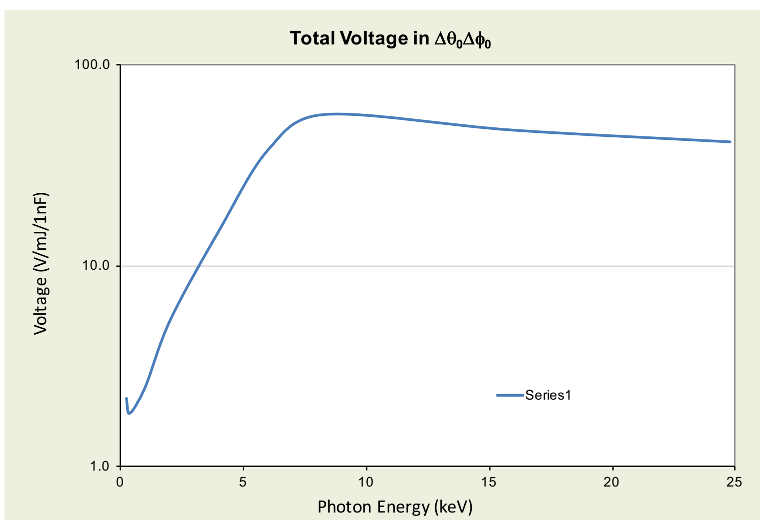

Figure 14. Total voltage generated in a diode in units of V, normalized to 1 mJ of FEL power and a 1nF collection capacitor (as the gain).

1.2.2.5. Shaping Amplifier

The charge pulse generated on the collection capacitor will be shaped before being digitized. The bandwidth of the amplifier needs to be sufficient to allow the 1 MHz operation. The noise performance must meet the 5% requirement for a dynamic range of 5 Volt, i.e. less than 250 mV rms, a very easy goal to achieve.

1.2.2.6. Analog-to-Digital Converter

Peak sensing ADC will be used to measure the pulse height after the shaping amplifier. The bandwidth of the ADC needs to be sufficient to allow the 1 MHz operation The noise performance must meet the 5% requirement for a dynamic range of 5 Volt, i.e. less than 250 mV rms, a very easy goal to achieve.

1.2.3. Possible Spurious Effect

1.2.3.1. Prompt Pulse

There have been experimental observations that when studying some electronic signals generated by an X-ray FEL beam interacting with certain material system, there was a prompt and ultra-fast single signal preceding the “real” signal of interest. The exact mechanism for this prompt signal has never been understood, but it is well separated from the main signal of interest, and in principle could be gated out. Measures should be taken to look and estimate the effect of this prompt signal, if exits, on the performance of the fault detection system being built for the collimators during the commissioning and subsequent operations.

1.3. Mechanical

The mechanical designs are referred to the engineering specification document.

1.4. Controls and Data Systems

The control and DAQ designs are referred to the engineering specification document.